

Wang, J., et al., 2024, Carbon cycling during the India-Asia collision revealed by  $\delta^{26}\text{Mg}$ – $\delta^{66}\text{Zn}$ – $\delta^{98}\text{Mo}$  evidence from ultrapotassic volcanoes in NW Tibet: *Geology*,  
<https://doi.org/10.1130/G52267.1>

## Supplemental Material

Methods, data, and supplemental figures.

# Supplemental Materials for

Carbon cycling during the India–Asia collision revealed by

$\delta^{26}\text{Mg}$ – $\delta^{66}\text{Zn}$ – $\delta^{98}\text{Mo}$  evidence from ultrapotassic volcanoes in

NW Tibet

Jian Wang<sup>1</sup>, Sebastian Tappe<sup>2</sup>, Qiang Wang<sup>1</sup>, Jie Li<sup>1</sup>, Zongqi Zou<sup>1</sup>, and Gong-Jian Tang<sup>1\*</sup>

<sup>1</sup>State Key Laboratory of Isotope Geochemistry, Guangzhou Institute of Geochemistry, Chinese Academy of Sciences, Guangzhou 510640, China

<sup>2</sup>Department of Geosciences, UiT The Arctic University of Norway, 9037 Tromsø, Norway

\*Corresponding author: G.-J. Tang ([tanggj@gig.ac.cn](mailto:tanggj@gig.ac.cn))

## Contents of this file

1. Analytical Methods
2. The petrography, elemental and isotopic compositions of the western Kunlun ultrapotassic volcanoes and the Kangxiwa mantle xenoliths
3. Effects of alteration, crustal contamination, and magmatic processes on Mg-Zn-Mo isotope systematics.
4. Details of Mg-Zn-Mo-Sr isotope modeling
5. Estimation of carbon (elemental C) input flux into the lithospheric mantle and volcanic CO<sub>2</sub> output flux into the atmosphere
6. Figures S1 to S11
7. Tables S1 to S9

## 1. Analytical methods

### *Mg-Zn-Mo isotope analyses*

All the samples were comminuted in a metal free environment to avoid Mg-Zn-Mo contamination from metal alloys, and finally were powdered to 200 mesh by using an agate mortar. Purification and isotopic analysis of Mg, Zn and Mo were performed respectively at the Ore Deposit and Exploration Centre, Hefei University of Technology, China, the Wuhan Sample Solution Analytical Technology Co., Ltd, Wuhan, China, and the State Key Laboratory of Isotope Geochemistry, Guangzhou Institute of Geochemistry, Chinese Academy of Sciences (SKLaBIG, GIG-CAS). All sample preparation and digestion work was undertaken in a Class 1000 clean laboratory equipped with Class 100 laminar-flow exhaust hoods. The analytical results are presented in [Table S1](#).

For Mg isotopes, approximately 10–20 mg of sample powders was weighed and then dissolved with a three-step procedure. Optima grade acids were added in the following sequence: (I) a mixture of concentrated HF and HNO<sub>3</sub> in a ratio of 2:1; (II) concentrated aqua regia (the mixture of HCl/HNO<sub>3</sub> in a ratio of 3:1); and (III) concentrated HNO<sub>3</sub>. Then, the beakers were heated on a hotplate at 125–135°C with caps on for 1–2 days. After digestion and drying, the samples were dissolved in 1 or 2 mL of 0.5 mol L<sup>-1</sup> HNO<sub>3</sub> for column chemistry. The detailed processes of column chromatography are the same as those described by [Huang et al. \(2021\)](#). In brief, the cation exchange resin (AG50W-X8) was backwashed and settled under gravity between each elution, followed by the cleaning procedure with 24 mL of 6 mol L<sup>-1</sup> double-distilled HCl and then 10 mL MQ-water. After conditioning with 5 mL of 0.5 mol L<sup>-1</sup> HNO<sub>3</sub>, samples were loaded in 400 µL of 0.5 mol L<sup>-1</sup> HNO<sub>3</sub>, then a combination of double-distilled 0.5 mol L<sup>-1</sup> HNO<sub>3</sub> and 1.0 mol L<sup>-1</sup> HNO<sub>3</sub> were used as the eluent to separate Mg. Magnesium

isotopic ratios were measured on a Thermo-Fisher Scientific Neptune-Plus multi-collector inductively coupled plasma mass spectrometer (MC-ICP-MS). A concentration-matched standard-sample bracketing technique was carried out to correct the instrumental drift and mass bias. A wet plasma was used with a quartz dual cyclonic-spray chamber and a 50  $\mu\text{L min}^{-1}$  PFA MicroFlow Teflon nebulizer (Elemental Scientific Inc., U.S.A.). A multicollector Faraday cup configuration of L3, C and H3 was used to measure  $^{24}\text{Mg}$ ,  $^{25}\text{Mg}$ , and  $^{26}\text{Mg}$ . The integration time of data acquisition was set to 2.097 s per cycle, with one block of 30 cycles for Mg isotope measurements. Cross-contamination between samples was eliminated by washing the sample-introduction system with 5% and 2%  $\text{HNO}_3$  for approximately 3 min. Magnesium isotope measurements were carried out in low resolution mode ( $M/\Delta M \sim 1200$ ). Usually, the separated Mg cuts were diluted to  $\sim 200$  ppb Mg solution in 2% (m/m)  $\text{HNO}_3$  to obtain a  $^{24}\text{Mg}$  intensity of approximately 7–8 V. The Mg isotopic compositions are expressed in standard notation in permil relative to standard reference material DSM-3:  $\delta^X\text{Mg}(\text{‰}) = [(^X\text{Mg}/^{24}\text{Mg})_{\text{sample}} / (^X\text{Mg}/^{24}\text{Mg})_{\text{DSM3}} - 1] \times 1000$ , where  $X = 25$  and  $26$ . The long-term external precision of  $\delta^{26}\text{Mg}$  is better than 0.06 ‰ (2SD), based on repeated analyses of reference materials and natural samples. To control analytical quality, each sample was measured at least 4 times and then averaged (Table S1). The rock standards BCR-2 and BHVO-2 were simultaneously processed with the samples to monitor accuracy and yielded  $\delta^{26/24}\text{Mg}$  values of  $-0.16\text{‰} \pm 0.07\text{‰}$  and  $-0.19 \pm 0.08\text{‰}$  (Table S1), respectively, consistent with those from previous studies (Teng et al., 2007; Wang et al., 2017). Repeated digestion and analysis of individual rock sample of 14QW100 yielded  $\delta^{26/24}\text{Mg}$  difference  $\leq 0.07\text{‰}$  (Table S1). The total procedural Mg blank during this study was less than 6 ng. The  $\delta^{26/24}\text{Mg}$  and  $\delta^{25/24}\text{Mg}$  values of all samples analyzed here fall onto a mass-dependent fractionation line with a slope of 0.5048 (Figure S1).

For Zn isotopes, approximately 50 mg of sample powders was weighed into in-house PTFE-lined steel bombs and dissolved in 1ml of concentrated HNO<sub>3</sub> and 1 ml of concentrated HF in the oven at 190°C for 48 hours. The digest contents were then dried and redissolved with 1 ml of concentrated HNO<sub>3</sub>. This step was repeated twice to completely remove HF. Then, 1 ml of concentrated HNO<sub>3</sub> and 2 ml MQ-water were added, and the bombs were screwed and placed in the oven overnight at 190°C. The digests were dried and redissolved with 1 ml of concentrated HCl to convert the sample from nitrate form to chloride form. Finally, the digests were evaporated to dryness and redissolved in 1ml of 8 mol L<sup>-1</sup> HCl + 0.001% H<sub>2</sub>O<sub>2</sub> in preparation for ion exchange separation. Zinc was purified by a single column ion-exchange chromatography using Bio-Rad strong anion resin AG-MP-1M (Zhu et al., 2019). In brief, 2 ml pre-cleaned resin was loaded onto the cleaned column. Matrix elements (e.g., K, Ca, Na, Mg, Al, Ti, Cr, Ni, and Mn) were eluted in the first 10 ml of 8 mol L<sup>-1</sup> HCl and Cu was collected in the following 24 ml of 8 mol L<sup>-1</sup> HCl + 0.001% H<sub>2</sub>O<sub>2</sub>. Then, after the Fe and Co were eluted by 12 ml of 0.5 mol L<sup>-1</sup> HCl, the Zn fraction was collected in 10 ml of 0.5 mol L<sup>-1</sup> HNO<sub>3</sub>. The recovery for Zn is >99%. The total procedural blanks are always <10 ng for Zn based on long-term analyses. The Zn fractions were evaporated to dryness, dissolved in 2% HNO<sub>3</sub>, and then re-evaporated to dryness and re-dissolved in 2% HNO<sub>3</sub> to remove all chlorine prior to isotope analysis. Zinc isotopic ratios were measured on a Thermo-Fisher Scientific Neptune-Plus MC-ICP-MS. Samples were introduced at a concentration of 200 ppb in 2% HNO<sub>3</sub> using wet plasma method. Standard-sample bracketing method was used in order to correct for instrumental mass fractionation. Zinc isotopic data are reported in standard notation in per mil relative to standard reference material JMC- 3-0749L:  $\delta^X\text{Zn}(\text{‰}) = [({}^X\text{Zn}/{}^{64}\text{Zn})_{\text{sample}}/({}^X\text{Zn}/{}^{64}\text{Zn})_{\text{JMC 3-0749L}} - 1] \times 1000$ , where X = 66 and 68. The long-term external precision of  $\delta^{66}\text{Zn}$  is better than 0.05 ‰ (2SD), based on repeated

analyses of reference materials and natural samples. To control analytical quality, each sample was measured at least 3 times and then averaged (Table S1). International standards JA-2 and BHVO-2 were simultaneously processed with the samples to monitor accuracy and yielded  $\delta^{66/64}\text{Zn}$  of  $0.29 \pm 0.04\text{‰}$  and  $0.30 \pm 0.02\text{‰}$  (Table S1), respectively, consistent with those from previous studies (Chen et al., 2016). Repeated digestion and analysis of individual rock sample of 14QW163 yielded  $\delta^{66/64}\text{Zn}$  difference  $\leq 0.04\text{‰}$  (Table S1). The  $\delta^{66/64}\text{Zn}$  and  $\delta^{68/64}\text{Zn}$  values of all samples analyzed here fall onto a mass-dependent fractionation line with a slope of 1.9543 (Figure S2).

For Mo isotopes, an appropriate mass of sample powder (50–400 mg) was weighed out to provide ~120 ng of Mo. About 120 ng of  $^{97}\text{Mo}$ – $^{100}\text{Mo}$  double spike solution was added before digestion of the samples. The sample-spike mixture was digested by using 4 ml of concentrated HF and 2 ml of concentrated  $\text{HNO}_3$  in closed beakers at  $120^\circ\text{C}$  for 48 hours. After digestion and drying, the samples were dissolved in 1 ml of concentrated HCl and then evaporated to dryness. The residue was redissolved in 2–4 ml of a mixture of  $0.1 \text{ mol L}^{-1} \text{ HF}/1 \text{ mol L}^{-1} \text{ HCl}$ , at which point it was ready for column separation. Molybdenum separation and purification were achieved using an extraction chromatographic resin of N-benzoyl-N-phenyl hydroxylamine manufactured in-house, following the protocols of Li et al. (2014). In brief, 0.5 ml of pre-cleaned resin was packed in a Poly-Prep column. A 2 ml aliquot of the sample solution was loaded onto the column, and the resin was washed with 8 ml of  $0.1 \text{ mol L}^{-1} \text{ HF}/1 \text{ mol L}^{-1} \text{ HCL}$ . Finally, the adsorbed Mo was eluted with 8 ml of  $6 \text{ mol L}^{-1} \text{ HF}/1 \text{ mol L}^{-1} \text{ HCl}$ . The Mo was collected in 15 ml PFA vials and evaporated to dryness on a hot plate at  $120^\circ\text{C}$ . Three drops of concentrated  $\text{HNO}_3$  and  $\text{H}_2\text{O}_2$  were added to the evaporated Mo to decompose any organic residue. Following this, 1 ml of 3%  $\text{HNO}_3$  was added to the Mo residue, after which the solution was ready for Mo

isotopic ratio measurement. Molybdenum isotope measurement was performed on a Thermo-Fisher Scientific Neptune-Plus MC-ICP-MS utilizing double spike analysis to correct for instrumental mass bias. The isotopic composition of Mo is expressed as  $\delta^{98/95}\text{Mo}$  relative to the NIST SRM 3134 standard:  $\delta^{98/95}\text{Mo}(\text{‰}) = (^{98}\text{Mo}/^{95}\text{Mo})_{\text{sample}} / (^{98}\text{Mo}/^{95}\text{Mo})_{\text{NIST SRM 3134}} - 1$ . The precision of Mo isotope ratio analyses was assessed by repeated measurements of NIST SRM 3134 ( $0.00\text{‰} \pm 0.05\text{‰}$ ,  $n=29$ ) (Table S2). The rock standards GBW07105 and AGV-2 were simultaneously processed with the samples to monitor accuracy and yielded  $\delta^{98/95}\text{Mo}$  values of  $-0.56\text{‰} \pm 0.07\text{‰}$  and  $-0.18 \pm 0.07\text{‰}$ , respectively (Table S1), consistent with those from previous studies (Willbold et al., 2016; Zhao et al., 2016). Molybdenum concentrations were calculated from spiked isotope measurements. The rock standards GBW07105 and AGV-2 gave a concentration of 3.00 ppm and 1.98 ppm, respectively (Table S1), also consistent with the values reported by the previous studies (Willbold et al., 2016; Zhao et al., 2016). Repeated digestion and analysis of individual rock sample of 14QW44 yielded  $\delta^{98/95}\text{Mo}$  difference  $\leq 0.06\text{‰}$  (Table S1). The total procedural blank for Mo was  $0.38 \pm 0.37$  ng (2SD,  $n=2$ ), far less than total Mo in the samples and standards.

### ***High-resolution 2-D elemental distribution maps***

High-resolution, two-dimensional, elemental X-ray mapping (Figure S6) was performed using a JEOL JXA-iSP100 Electron Probe Microanalyzer equipped with five wavelength-dispersive spectrometers (WDS) at the Laboratory of Guangzhou Tuoyan Analytical Technology Co., Ltd. Operating conditions for the X-ray mapping involved an accelerating voltage of 20 kV, a beam current of 100 nA, a step size of 1  $\mu\text{m}$  and dwell time of 30 ms. Si and Mg were analyzed using a TAP crystal. K was analyzed with a PETL crystal. Ca was analyzed with a PETJ crystal.

Fe was analyzed using a LIFH crystal. Elemental K $\alpha$  line was chosen for Si, Mg, K, Ca and Fe during analyses.

### *Raman spectroscopic measurements*

Raman spectra of representative calcite and CO<sub>2</sub> bubble inclusions in clinopyroxene from the Kangxiwa mantle xenoliths were obtained using a WITec alpha300 R confocal Raman spectrometer at the SKLaBIG, GIG-CAS, using a 532-nm laser, a 300-mm<sup>-1</sup> grating, a 100× Zeiss objective, and a back-illuminated charged-coupled detector (1600 × 200 pixels). The Raman spectrometer was calibrated using a standard silicon wafer. Spot Raman spectra from the inclusions were acquired by averaging 5–10 acquisition sequences, with acquisition times of 100 s per sequence. Raman spectra were processed using the Control Five software. The analytical results are presented in [Table S3](#).



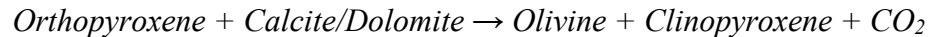
## 2. The petrography, elemental and isotopic compositions of the western Kunlun ultrapotassic volcanoes and the Kangxiwa mantle xenoliths

### *Ultrapotassic volcanoes*

Ultrapotassic volcanic activities have been widely identified in the western Kunlun area, probably representing the youngest magmatism in the Tibetan Plateau (Guo et al., 2019; Wang et al., 2023). The ages of these volcanoes range from ~8.3 Ma to the present, with a decreasing trend from south to north (Figure S3). Representative ultrapotassic samples were collected from the Kangxiwa, Dahongliutan, Quanshuigou, and Keliya areas (Figure S3). Petrographic examination reveals no evidence of hydrothermal or weathering modification in these rocks (Figure S4). These samples range in composition from basalt to dacite and exhibit porphyritic textures (Figure S7). The phenocrysts (~10–15 vol %) mainly comprise clinopyroxene, plagioclase, phlogopite, olivine, and accessory orthopyroxene and K-feldspar. They have higher K<sub>2</sub>O contents (2.52–5.87 wt %, mean=4.74 wt %) relative to Na<sub>2</sub>O (2.31–5.12 wt %, mean=3.54 wt %) (Table S4). The western Kunlun ultrapotassic lavas display arc-like trace-element patterns and remarkably enriched Sr–Nd–Pb–Hf isotope compositions that closely resemble the EM2 mantle end-member represented by the Samoan hotspot (Figure S8–S9). These features indicate that their mantle source contain recycled sedimentary materials (with compositions comparable to the upper continental crust) (Jackson et al., 2007; Wang et al., 2023). The ultrapotassic lavas exhibit lower  $\delta^{26}\text{Mg}$  (–0.39‰ to –0.19 ‰) and higher  $\delta^{66}\text{Zn}$  (+0.27‰ to +0.36‰) values (Figure 3). Their  $\delta^{98}\text{Mo}$  values range from –0.78‰ to 0‰ (Figure 3). The varying Mg–Zn–Mo isotopic compositions across different locations likely indicate different proportions of recycled carbonate-rich sediments in the mantle source, accompanied by minor crustal contamination (<10%) (Figure 3).

## *Mantle xenoliths*

Mantle xenoliths entrained in the Kangxiwa ultrapotassic lavas are small with diameters generally ranging from 0.5 to 1.5 cm (Figure S4). These xenoliths, primarily lherzolite, appear fresh and consist of olivine, orthopyroxene, clinopyroxene, and spinel (Figure S4). In addition, they contain abundant primary carbonate minerals, mainly dolomite and calcite (Figure S5). These carbonates coexist with clinopyroxene, occurring either interstitially or as mineral inclusions (Figure S5). Dolomite is generally subhedral to euhedral in shape and can reach size of up to 300  $\mu\text{m}$ , whereas calcite is less common and typically smaller in size (Figure S5). Furthermore, clinopyroxene typically contains  $\text{CO}_2$  bubbles (Figure S5), consistent with carbonate metasomatism via interactions between peridotitic mantle and  $\text{CaCO}_3$ -rich melts/fluids, according to the following reaction:



Clinopyroxenes in the mantle xenoliths exhibit enriched  $^{87}\text{Sr}/^{86}\text{Sr}$  ratios (0.7095-0.7113), consistent with those of the western Kunlun ultrapotassic lavas (0.7080-0.7100) (Figure 3) (Tables S4-S5). This suggests a genetic link between the mantle xenoliths and the ultrapotassic lavas, demonstrating that the latter originated from a lithospheric mantle.

### 3. Effects of alteration, crustal contamination, and magmatic processes on Mg-Zn-Mo isotope systematics.

#### *Alteration*

The studied ultrapotassic lavas are fresh with low LOI (<3 wt. %) (Table S4). There are no correlations between Mg-Zn isotope data and LOI (Figure S11), indicating that alteration did not affect the Mg-Zn isotope data. However, there is a negative correlation between  $\delta^{98}\text{Mo}$  and LOI, which indicates that Mo isotope data may have more or less been mobilized. The variations of  $\delta^{98}\text{Mo}$  may be not related to alteration but possibly resulted from some other mechanism (e.g., fluid migration during subduction). This is because weathering-related Mo depletion would cause a negative correlation between Ce/Mo and Ba/Th ratios (Huang et al., 2023), which is not observed in the studied ultrapotassic lavas (Figure S11). Thus, we suggest that alteration did not significantly affect the Mg-Zn-Mo isotope data.

#### *Crustal contamination*

Mantle-derived magmas may be subject to some degree of crustal contamination on their way to the surface. The significant crustal thickness (>50 km) of the Tibetan Plateau increases the possibility of magmas being contaminated by crustal materials. However, there are no correlations between  $\text{SiO}_2$  and Sr-Nd-Pb-Hf isotopic ratios (Figure 10), indicating that crustal contamination is negligible in the generation of the western Kunlun ultrapotassic lavas. In addition, the studied ultrapotassic lavas have  $\delta^{98}\text{Mo}$  (-0.78‰ to 0‰) values much lower than the average continental crust ( $\delta^{98}\text{Mo}$  of +0.10‰ to +0.35‰, Willbold and Elliott, 2017), precluding significant crustal contamination. Mg-Zn-Mo-Sr isotopic modeling further reveals that the ultrapotassic magmas were contaminated by Indian crustal components by less than 10% (Figure

3). It is noted that the Keliya samples exhibit more radiogenic  $^{87}\text{Sr}/^{86}\text{Sr}$  ratios than other locations (Figure 3), suggesting a relatively higher degree of crustal contamination.

### ***Magmatic processes***

The western Kunlun ultrapotassic lavas have experienced olivine, clinopyroxene and plagioclase fractionation (Wang et al., 2023). However, there are no correlations between the Mg-Zn-Mo isotope data and geochemical parameters such as Mg#, Ni,  $\text{CaO}/\text{Al}_2\text{O}_3$  and Eu (Figure S11). Thus, it can be ruled out that fractional crystallization (e.g., olivine, clinopyroxene and plagioclase) processes affected the Mg-Zn-Mo isotopic compositions of the ultrapotassic lavas.

Previous studies have suggested that varying degrees of partial melting of the mantle could lead to Mg-Zn-Mo isotopic fractionation (Doucet et al., 2016; Teng et al., 2017; McCoy-West et al., 2019; Day et al., 2022). A weak correlation between  $\delta^{98}\text{Mo}$  and La/Sm (a proxy for the degree of partial melting) is observed (Figure S11), suggesting that partial melting may have caused Mo isotopic fractionation in the studied ultrapotassic lavas. Large-degree (10–15%) partial melts of the depleted mantle (i.e., MORBs) have slightly heavier  $\delta^{98}\text{Mo}$  values than the average chondritic value ( $-0.14\text{‰} \pm 0.02\text{‰}$ ), and thus Liang et al. (2017) suggested that Mo isotopic fractionation is limited ( $\Delta\delta^{98}\text{Mo} < 0.15\text{‰}$ ) during moderate degrees of partial melting. However, the studied ultrapotassic lavas formed by much lower degrees of partial melting ( $< 5\%$ ) (Wang et al., 2023) and display significant  $\delta^{98}\text{Mo}$  variations of  $0.78\text{‰}$ . This suggests that partial melting alone cannot explain the variable  $\delta^{98}\text{Mo}$  measured. Based on this evidence and the absence of a correlation between Mg-Zn isotope data and La/Sm (Figure S11), we suggest that partial melting did not significantly impact the Mg-Zn-Mo isotopic compositions of the ultrapotassic lavas.

234           In summary, we suggest that the  $\delta^{26}\text{Mg}$ – $\delta^{66}\text{Zn}$ – $\delta^{98}\text{Mo}$  compositions of the western  
235 Kunlun ultrapotassic lavas are inherited mainly from their mantle source.

236

#### 4. Details of Mg-Zn-Mo-Sr isotope modeling

Mantle carbonatite metasomatism is modeled by binary mixing between normal mantle-derived melts (MORB) and carbonate melts (calcite, dolomite and magnesite) (Figure 3). Crustal contaminant is modeled by binary mixing between normal mantle-derived melts (MORB) and Indian continental crust (Figure. 3). The equation of the above modeling is expressed by:

$$I_{cm} = I_{ca} * (C_a * X / C_m) + I_{cb} * [C_b * (1 - X) / C_m]$$

Where  $C_a$ ,  $C_b$ , and  $C_m$  are the concentration of an element in endmember a, in endmember b, and in mixed endmember resulted from mixing of endmembers a and b, respectively.  $X$  (0–100%) is the degree of mixing.  $I_{ca}$ ,  $I_{cb}$ , and  $I_{cm}$  are the isotopic ratio of any endmember in magma a, endmember b, and in mixed endmember resulting from mixing of endmembers a and b, respectively.

Details about the trace element and isotope data for end-members used in geochemical modeling are presented in Table S7.

## 5. Estimation of carbon (elemental C) input flux into the lithospheric mantle and volcanic CO<sub>2</sub> output flux into the atmosphere

To estimate the input flux of recycled carbon (elemental C)  $M_{input}$  (C, Mt/yr) into the lithospheric mantle and output flux of volcanic CO<sub>2</sub> into the atmosphere  $M_{output}$  (CO<sub>2</sub>, Mt/yr), we use the Monte Carlo modeling following method described by [Shu et al. \(2023\)](#). The basic principles and formulas for the Monte Carlo modeling are described below:

$$(1) M_{input} (C, Mt/yr) = (\alpha * \beta * X * \gamma * \lambda * \omega_c * \omega_{cc} * \rho) / \mu$$

$$(2) M_{output} (CO_2, Mt/yr) = M_{input} * \varepsilon * 44/12$$

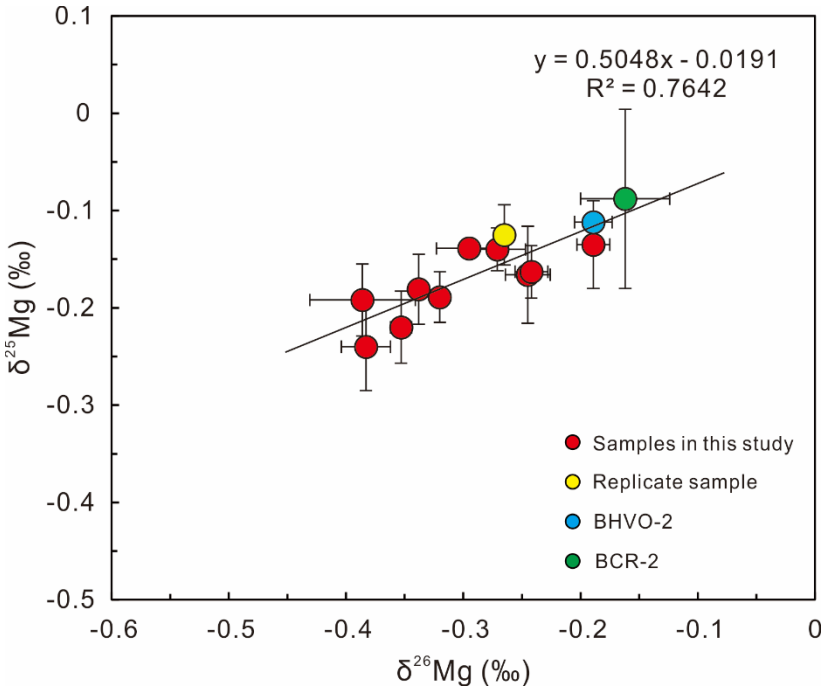
In Equation (1), where  $\alpha$  and  $\beta$  represent the length (600 km) and width (300 km) of the studied region,  $X$  is the thickness of the metasomatized lithospheric mantle (1–80 km) in NW Tibet,  $\gamma$  (10%–50%) is the percentage by area of the mantle that has been metasomatized ([Shu et al., 2023](#)),  $\lambda$  (0%–50%) is the mass fraction of carbonate-rich sediment melts calculated in [Figure 3](#),  $\omega_c$  (10%–50%) is the proportion of carbonates in the carbonate-rich sediments,  $\omega_{cc}$  (12%) is the mass fraction of C in carbonates (assumed to be calcite),  $\rho$  ( $2.4 * 10^{15}$  g/km<sup>3</sup>) is the density of carbonate melts in the upper mantle ([Ritter et al., 2020](#)) and  $\mu$  is the initial eruption ages (~8.3 Ma) of the ultrapotassic lavas in the western Kunlun area ([Guo et al., 2019](#); [Wang et al., 2023](#)). In Equation (2), where  $\varepsilon$  (60%–90%) is the rational recycling efficiency of subducted carbon to the atmosphere through subaerial volcanoes ([Plank and Manning, 2019](#)). The detailed Monte Carlo modeling results are presented in [Tables S8-S9](#). We acknowledge the large uncertainties associated with Monte Carlo modeling for CO<sub>2</sub> fluxes ([Table S9](#)), primarily due to the large uncertainties in input parameters ([Table S8](#)). However, we contend that our modeling approach is reasonable. This is based not only on the selection of reasonable input parameters but also on the alignment of the simulated emission rates with observed outputs from dominant

274 volcanic fields in NW Tibet as well as independent estimate from the Sr-Nd-Pb isotope mass  
275 balance ([Guo et al., 2021](#)). Thus, our estimates provide an important reference for future studies.

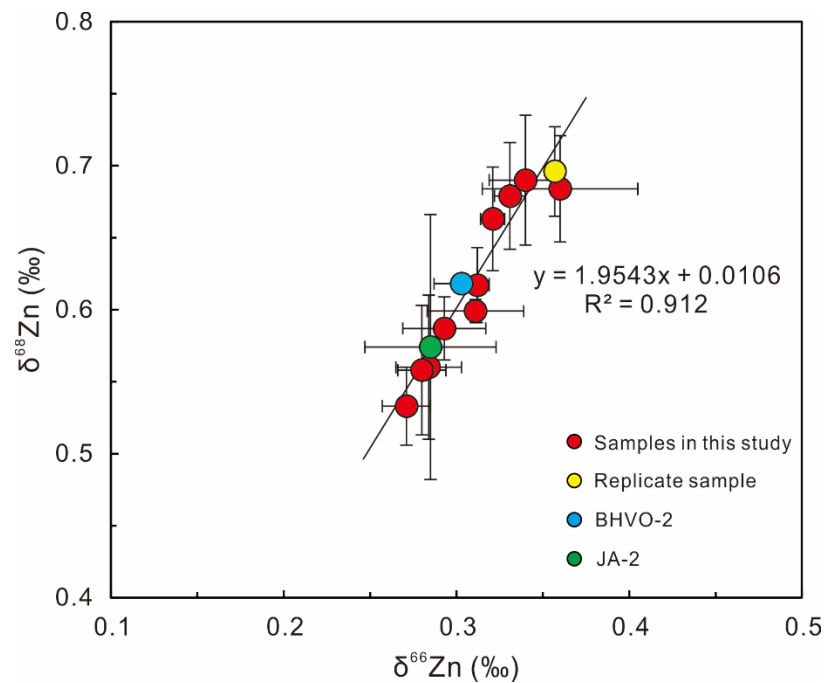
276



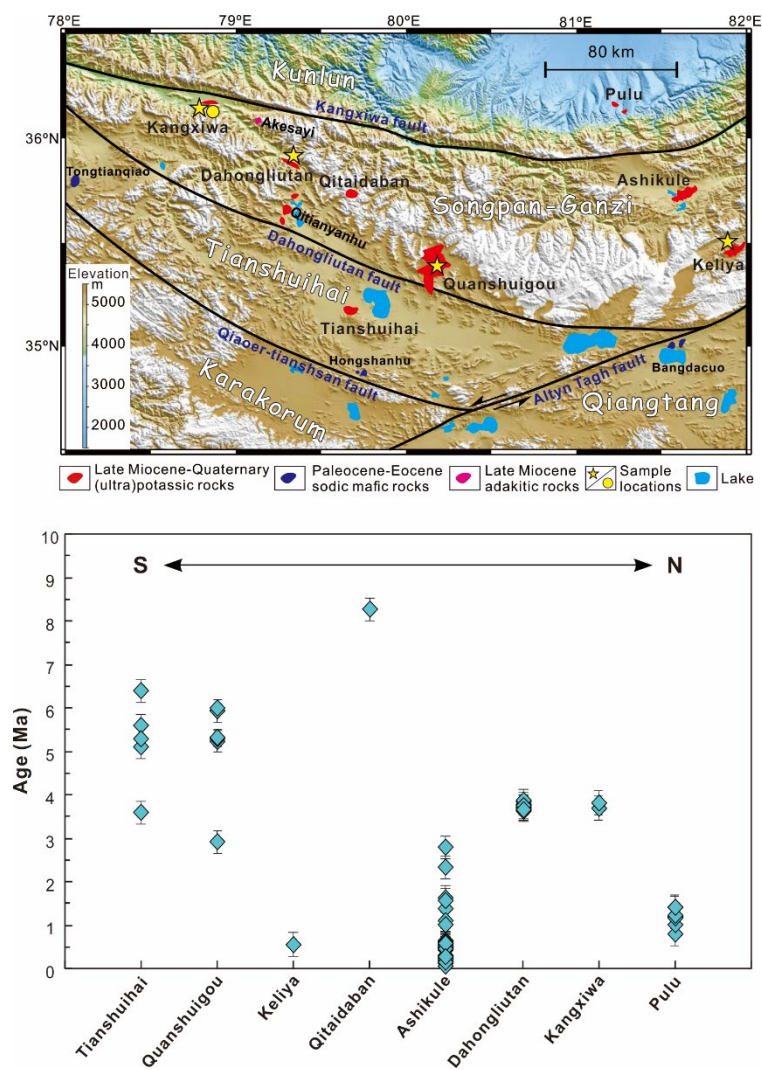
277 **Figure S1.** Relationship between measured  $\delta^{25}\text{Mg}$  and  $\delta^{26}\text{Mg}$  values for ultrapotassic volcanoes  
278 in NW Tibet and standard materials. All samples analyzed define the mass fractionation line with  
279 a slope of 0.5048, indicating that there are no analytical artifacts from unresolved isobaric  
280 interferences on measured Mg isotopic ratios.



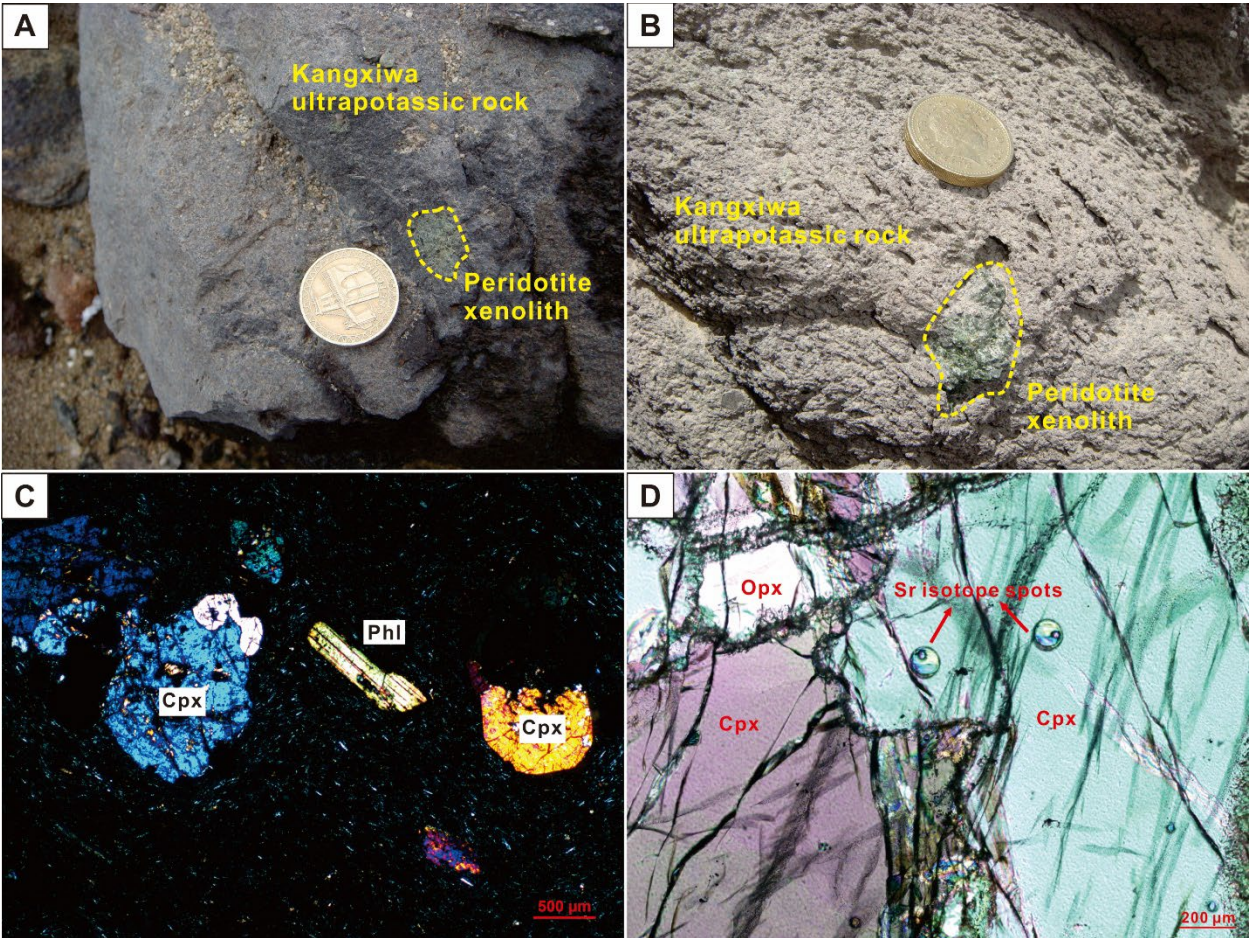
283 **Figure S2.** Relationship between measured  $\delta^{68}\text{Zn}$  and  $\delta^{66}\text{Zn}$  values for ultrapotassic volcanoes in  
284 NW Tibet and standard materials. All samples analyzed define the mass fractionation line with a  
285 slope of 1.9543, indicating that there are no analytical artifacts from unresolved isobaric  
286 interferences on measured Zn isotopic ratios.



289 **Figure S3.** Spatio-temporal distribution of ultrapotassic volcanoes from the western Kunlun area  
 290 of NW Tibet (after [Guo et al., 2019](#), [Tang et al., 2022](#) and [Wang et al., 2023](#)).

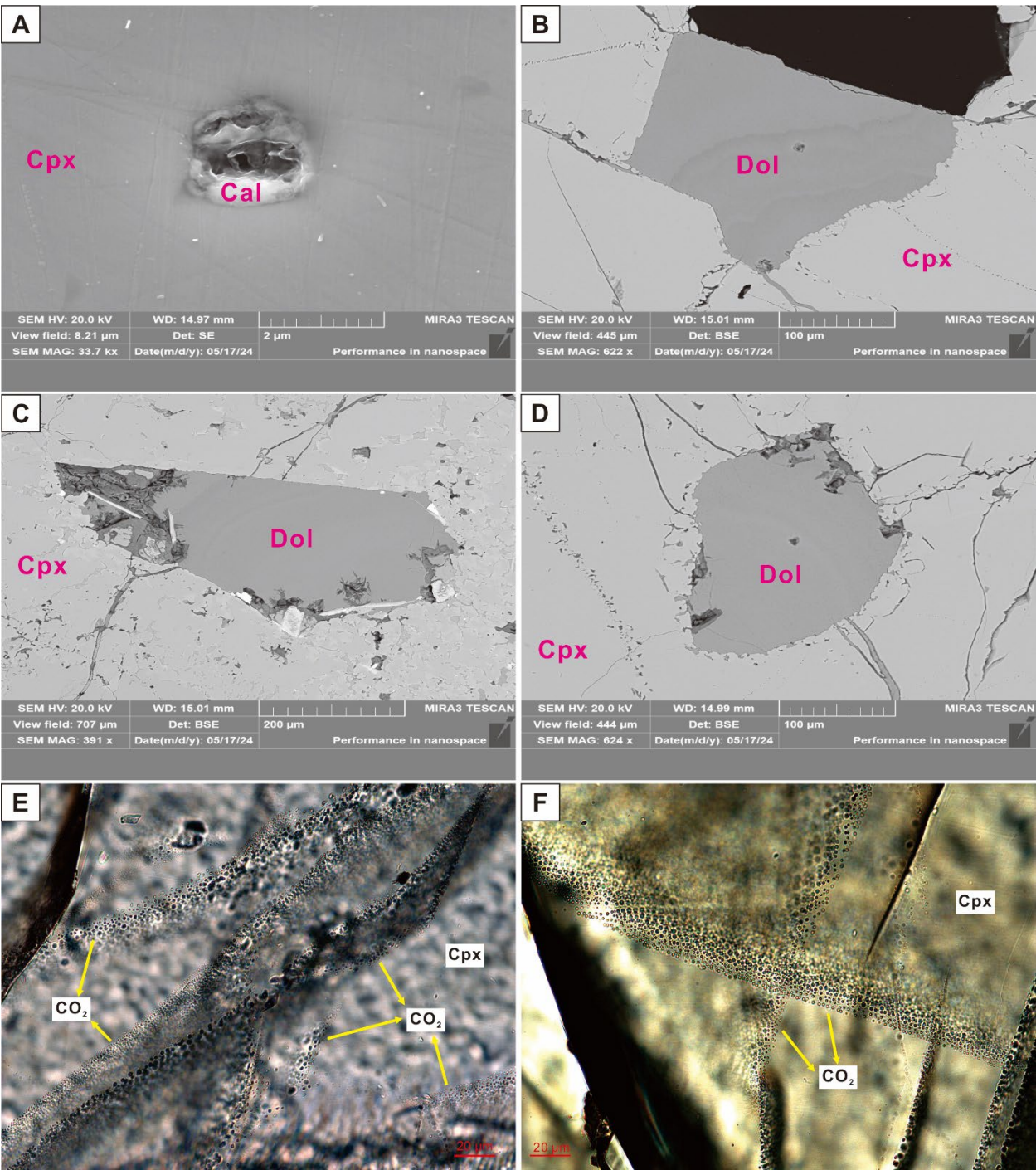


293 **Figure S4.** (A-B) Field photos of mantle xenoliths in the Kangxiwa ultrapotassic lavas; (C)  
294 photomicrograph (orthogonal light) of the Kangxiwa ultrapotassic lavas; (d) photomicrograph  
295 (orthogonal light) of the Kangxiwa mantle xenoliths; Cpx=clinopyroxene; Phl=phlogopite;  
296 Opx=orthopyroxene. The Sr isotope spots of clinopyroxene were analyzed by [Tang et al. \(2022\)](#),  
297 and the data are listed in [Table S5](#).



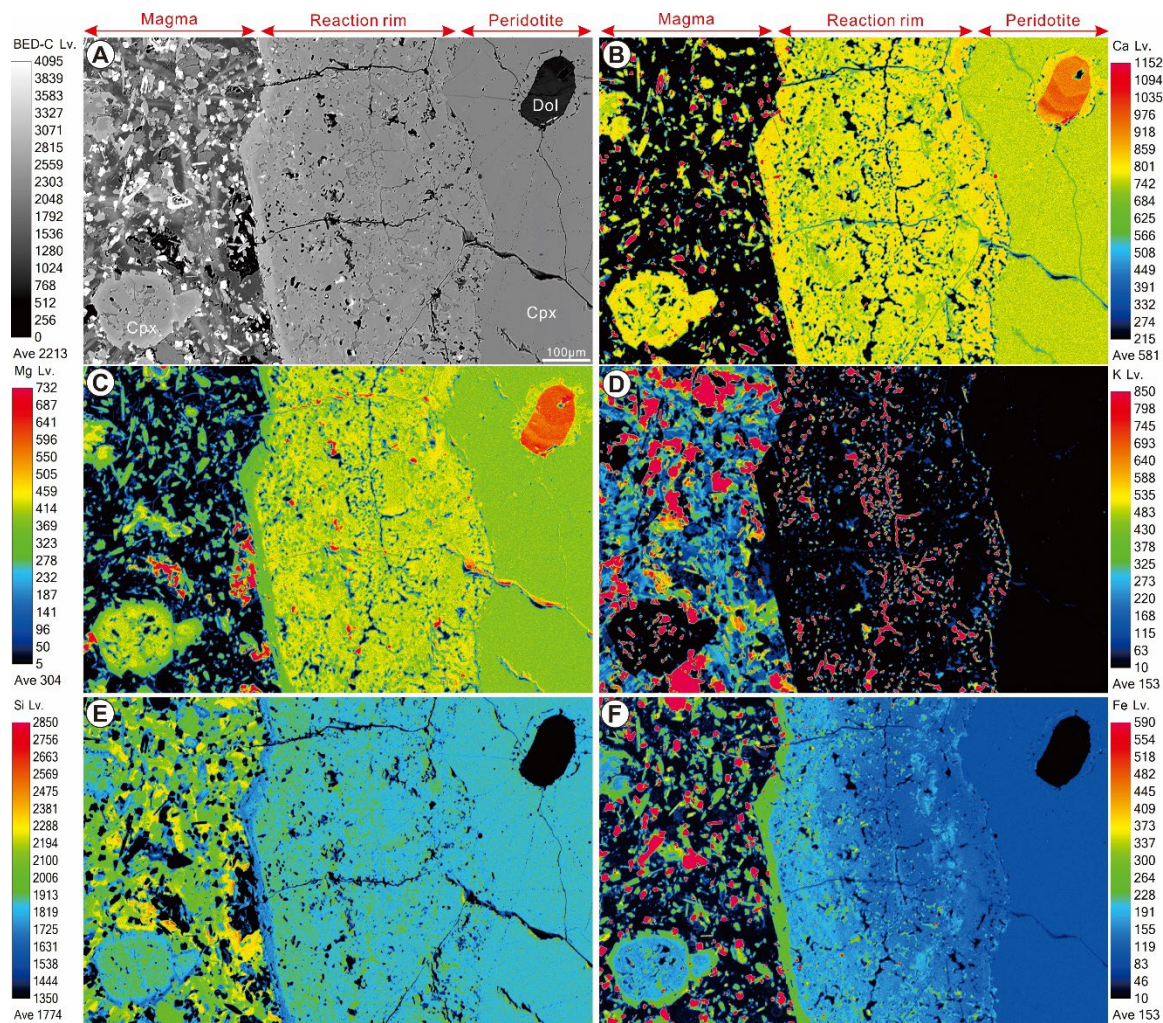


300 **Figure S5.** (A-D) BSE images of carbonate minerals in the clinopyroxene from the Kangxiwa  
 301 mantle xenoliths; (E-F) Photomicrograph (transmission light) of abundant CO<sub>2</sub> bubbles in the  
 302 clinopyroxene of the Kangxiwa mantle xenoliths. Cpx=clinopyroxene; Cal=calcite; Dol=  
 303 dolomite.

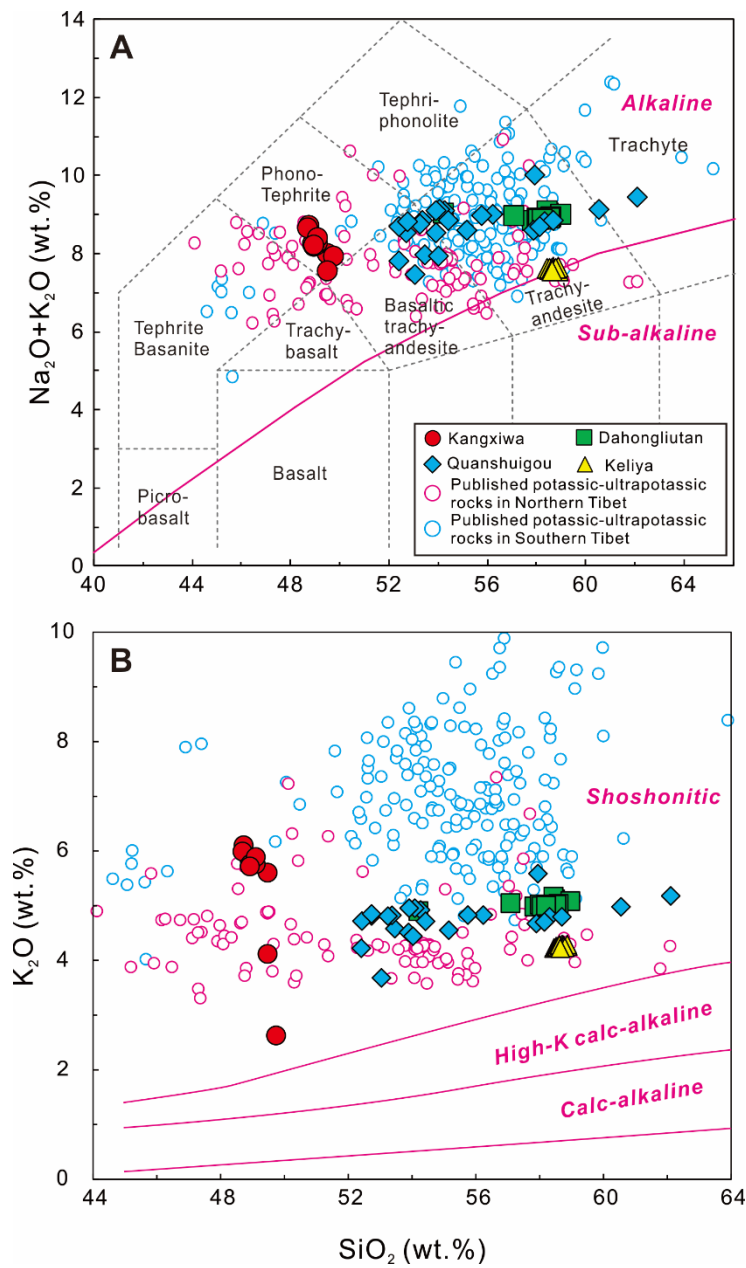




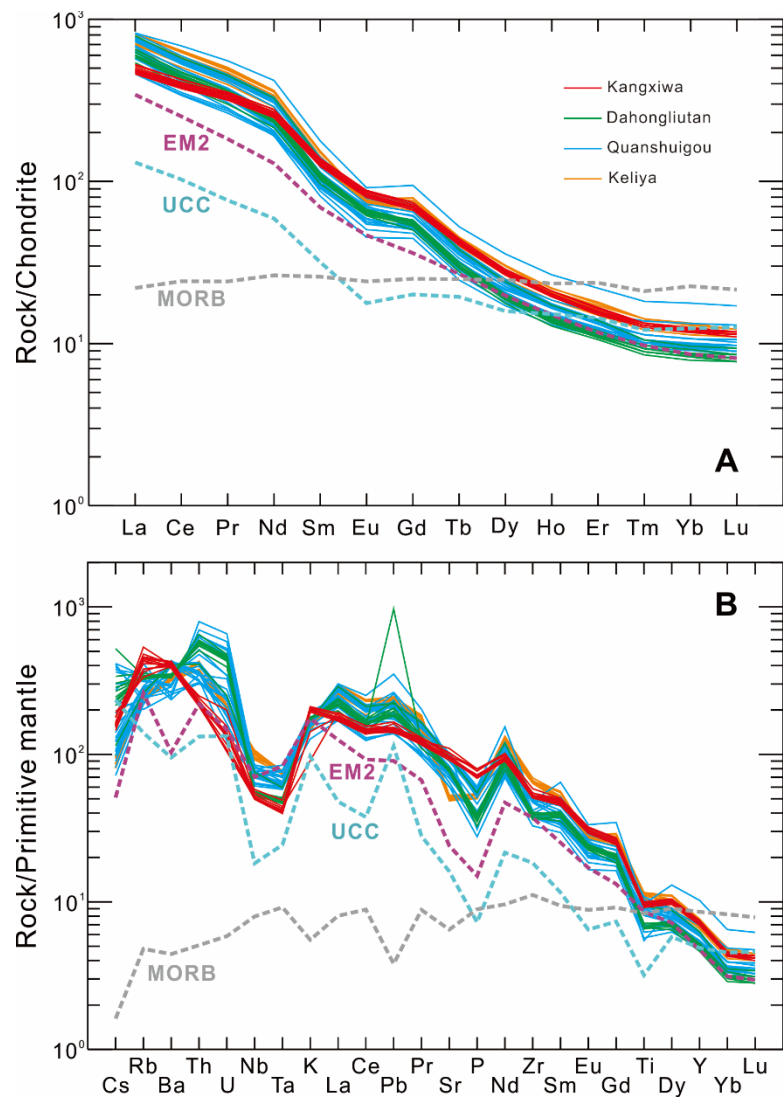
305 **Figure S6.** (A) BSE and (B-F) EPMA elemental (e.g., Ca, Mg, K, Si and Fe) X-ray maps of  
306 peridotite xenoliths in the Kangxiwa ultrapotassic lavas. Cpx=clinopyroxene; Dol=Dolomite.



309 **Figure S7.** (A) Total alkalis vs  $\text{SiO}_2$  and (B)  $\text{K}_2\text{O}$  vs  $\text{SiO}_2$  for the studied ultrapotassic lavas from  
 310 the western Kunlun area of NW Tibet. Published data sources for Cenozoic ultrapotassic rocks  
 311 from Northern Tibet and Southern Tibet can be found in [Wang et al. \(2023\)](#).



314 **Figure S8.** (A) Chondrite-normalized REE patterns and (B) primitive mantle-normalized spider  
 315 diagrams for the studied ultrapotassic lavas from the western Kunlun area of NW Tibet.  
 316 Normalizing values are from [McDonough et al. \(1995\)](#). Also shown are typical end-member  
 317 reservoirs, including enrich mantle-2 (EM2, Samoan) ([Jackson et al., 2007](#)), UCC ([Rudnick and](#)  
 318 [Gao, 2014](#)), and MORB ([Gale et al., 2013](#)).





321 **Figure S9.** (A)  $^{143}\text{Nd}/^{144}\text{Nd}$  vs.  $^{87}\text{Sr}/^{86}\text{Sr}$ , (B)  $\epsilon_{\text{Hf}}$  vs.  $\epsilon_{\text{Nd}}$ , (C)  $^{87}\text{Sr}/^{86}\text{Sr}$  vs.  $^{206}\text{Pb}/^{204}\text{Pb}$  and (D)

322  $^{143}\text{Nd}/^{144}\text{Nd}$  vs.  $^{206}\text{Pb}/^{204}\text{Pb}$  for the studied ultrapotassic lavas from the western Kunlun area of

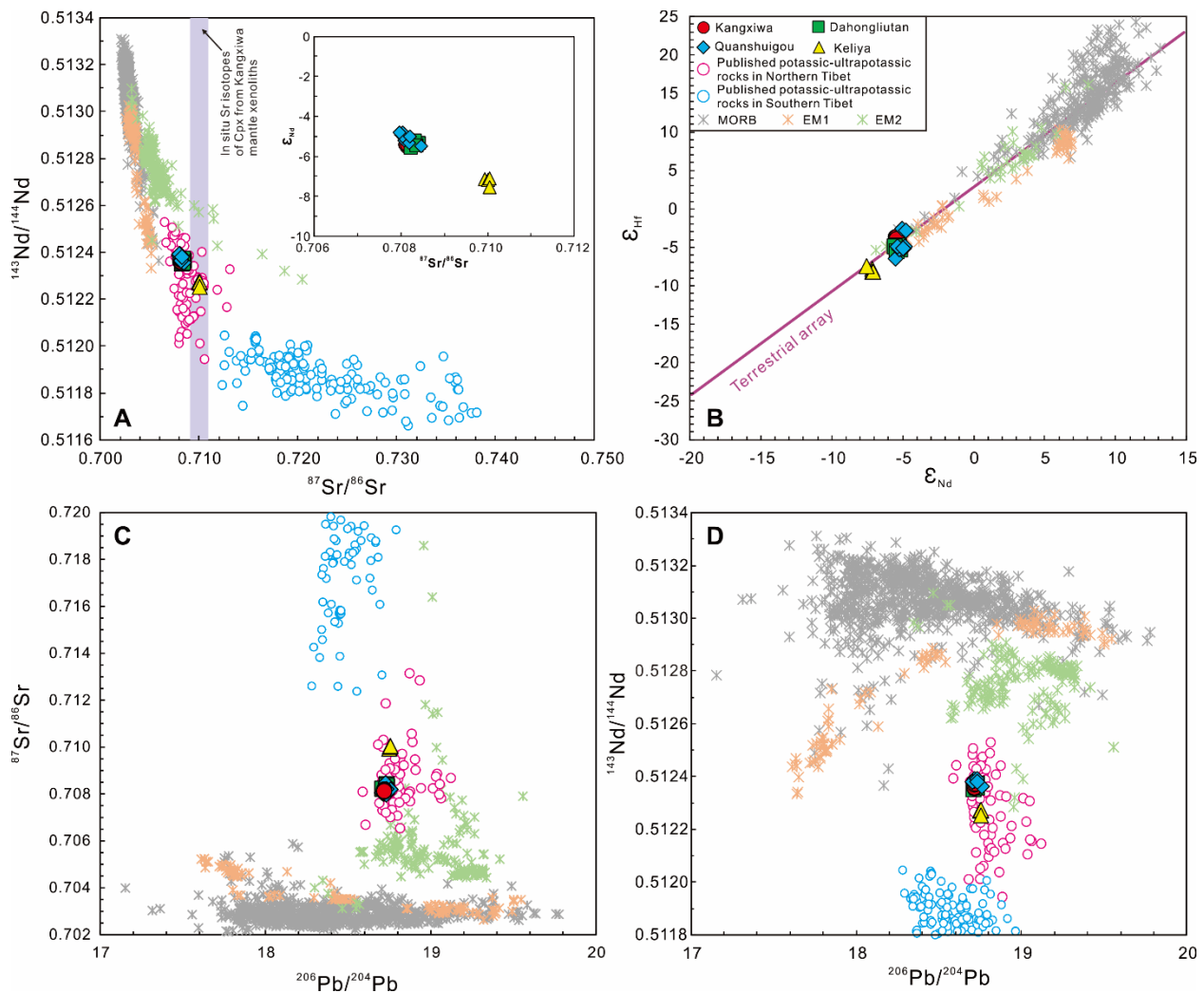
323 NW Tibet. Published data sources for Cenozoic ultrapotassic rocks from Northern Tibet and

324 Southern Tibet can be found in Wang et al. (2023). Data sources for Sr isotope of clinopyroxenes

325 from Kangxiwa mantle xenoliths are from Tang et al. (2022). Data sources for MORB, EM1

326 (Pitcairn) and EM2 (Samoa) are from <http://georoc.mpch-mainz.gwdg.de/georoc/>. In (B), The

327 terrestrial array ( $\epsilon_{\text{Hf}} = 1.36 \cdot \epsilon_{\text{Nd}} + 2.95$ ) is referenced from Vervoort et al. (1999).



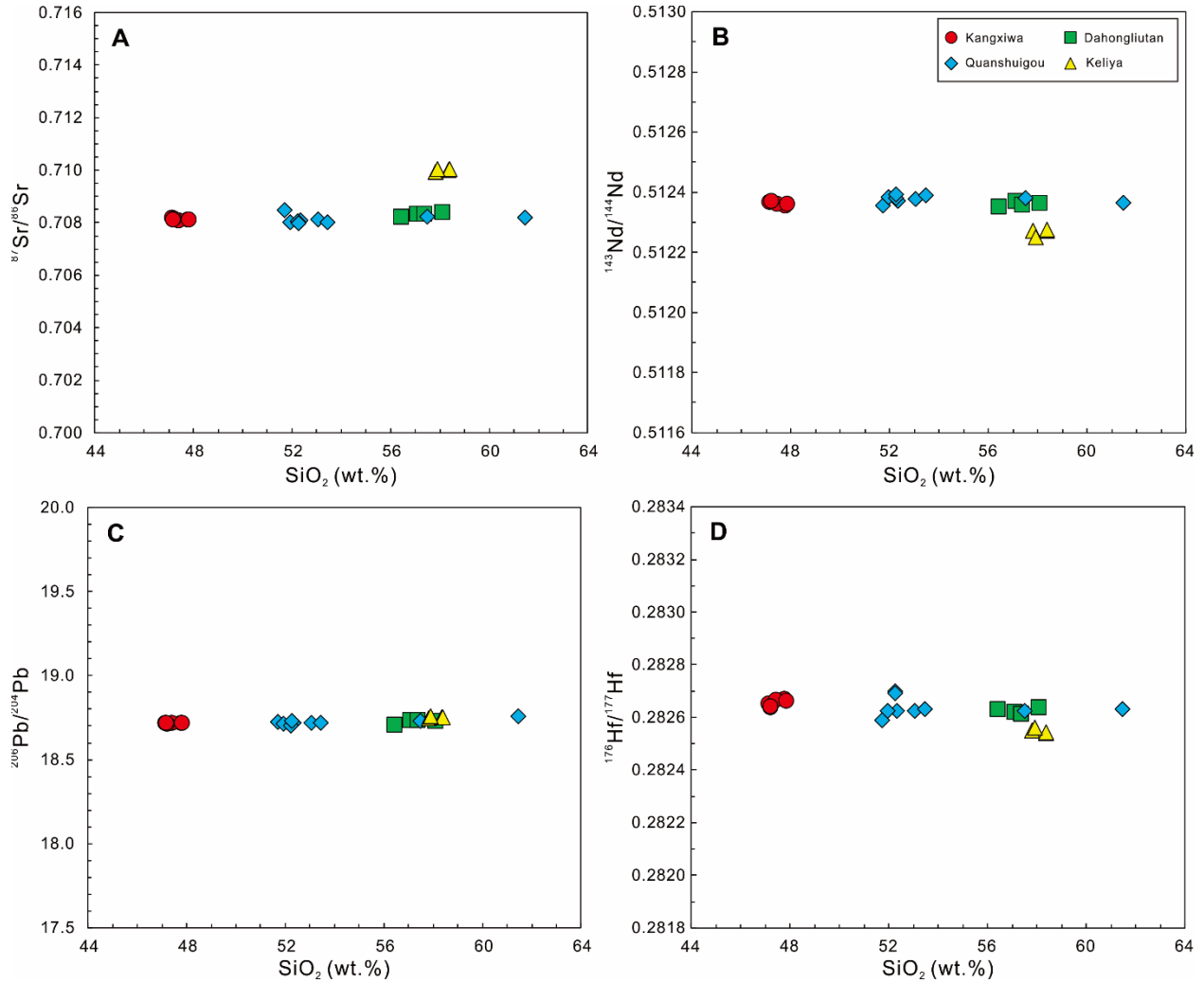
330 **Figure S10.** (A)  $^{87}\text{Sr}/^{86}\text{Sr}$  vs.  $\text{SiO}_2$ , (B)  $^{143}\text{Nd}/^{144}\text{Nd}$  vs.  $\text{SiO}_2$ , (C)  $^{206}\text{Pb}/^{204}\text{Pb}$  vs.  $\text{SiO}_2$ , and (D)

331  $^{176}\text{Hf}/^{177}\text{Hf}$  vs.  $\text{SiO}_2$  for the studied ultrapotassic lavas from the western Kunlun area of NW

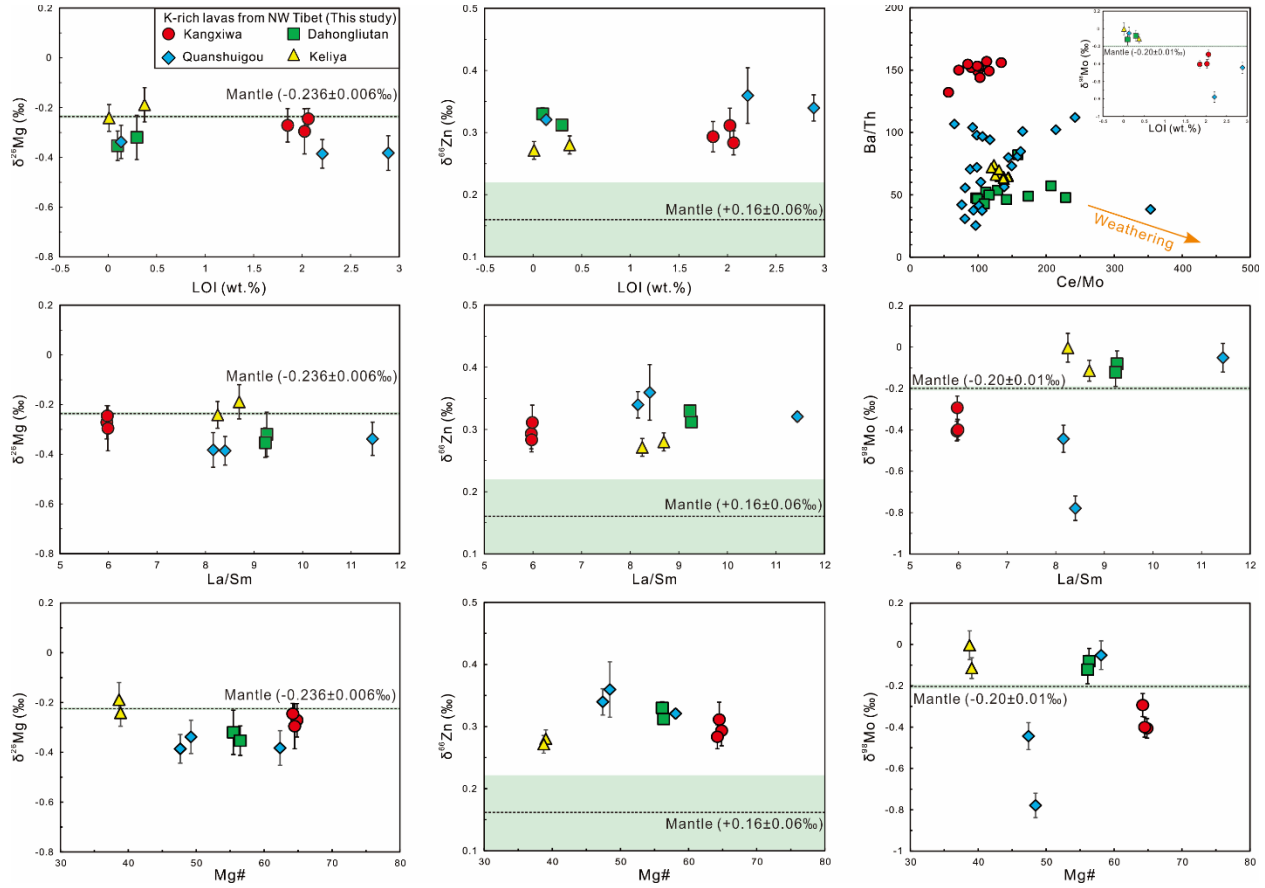
332 Tibet. There are no correlations between  $\text{SiO}_2$  and Sr-Nd-Pb-Hf isotopic ratios, indicating that

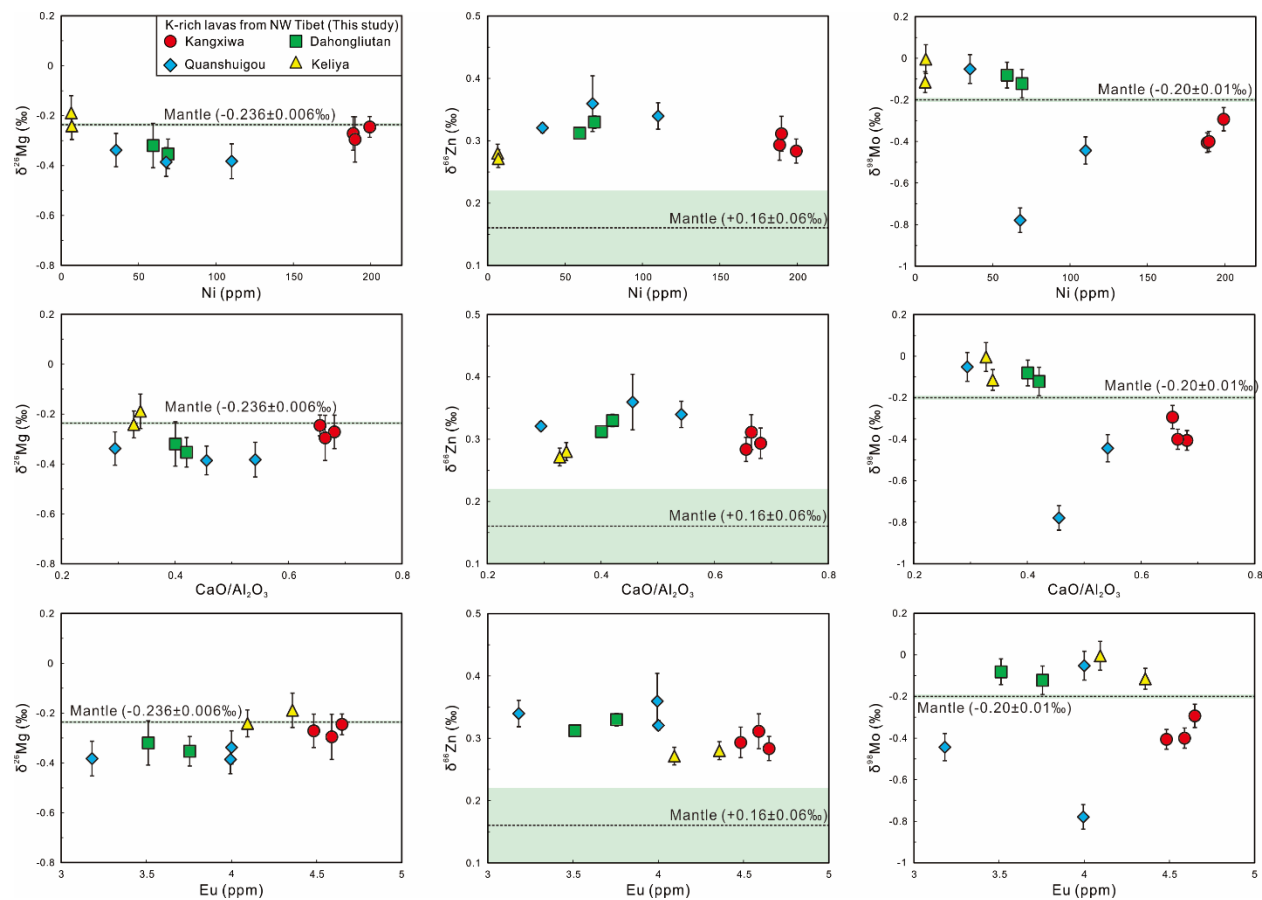
333 crustal contamination is negligible in the generation of the studied ultrapotassic

334 lavas.



337 **Figure S11.** Plots of Mg-Zn-Mo isotopes vs. LOI, La/Sm, Mg#, Ni, CaO/Al<sub>2</sub>O<sub>3</sub> and Eu for the  
 338 Cenozoic ultrapotassic lavas from the western Kunlun area of NW Tibet. Plot of Ba/Th vs  
 339 Ce/Mo for the studied ultrapotassic lavas. The green area represents normal mantle  $\delta^{26}\text{Mg}$  (-  
 340  $0.236\pm0.006\text{‰}$ ) (Liu et al., 2023),  $\delta^{66}\text{Zn}$  ( $+0.16\pm0.06\text{‰}$ ) (Sossi et al., 2018) and  $\delta^{98}\text{Mo}$  (-  
 341  $0.20\pm0.01\text{‰}$ ) (McCoy-West et al., 2019) values.





## REFERENCES CITED

- Bezard, R., Fischer-Gödde, M., Hamelin, C., Brennecke, G. A., and Kleine, T., 2016, The effects of magmatic processes and crustal recycling on the molybdenum stable isotopic composition of Mid-Ocean Ridge Basalts: *Earth and Planetary Science Letters*, v. 453, p. 171–181. <https://doi.org/10.1016/j.epsl.2016.07.056>.
- Chen, S., Liu, Y., Hu, J., Zhang, Z., Hou, Z., Huang, F., and Yu, H., 2016, Zinc isotopic compositions of NIST SRM 683 and whole-rock reference materials: *Geostandards and Geoanalytical Research*, v. 40, p. 417–432, <https://doi.org/10.1111/j.1751-908X.2015.00377.x>.
- Chen, S., Hin, R. C., John, T., Brooker, R., Bryan, B., Niu, Y., and Elliott, T., 2019, Molybdenum systematics of subducted crust record reactive fluid flow from underlying slab serpentine dehydration: *Nature Communications*, v. 10, p. 4773, <https://doi.org/10.1038/s41467-019-12696-3>.
- Chen, S., Sun, P., Niu, Y., Guo, P., Elliott, T., and Hin, R. C., 2022, Molybdenum isotope systematics of lavas from the East Pacific Rise: Constraints on the source of enriched mid-ocean ridge basalt: *Earth and Planetary Science Letters*, v. 578, p. 117283, <https://doi.org/10.1016/j.epsl.2021.117283>.
- Day, J. M. D., Moynier, F., and Ishizuka, O., 2022, A partial melting control on the Zn isotope composition of basalts: *Geochemical Perspectives Letters*, v. 23, p. 11–16, 10.7185/geochemlet.2230.
- Doucet, L. S., Mattielli, N., Ionov, D. A., Debouge, W., and Golovin, A. V., 2016, Zn isotopic heterogeneity in the mantle: A melting control?: *Earth and Planetary Science Letters*, v. 451, p. 232–240, 10.1016/j.epsl.2016.06.040.
- Fan, J.-J., Wang, Q., Li, J., Wei, G.-J., Ma, J.-L., Ma, L., Li, Q.-W., Jiang, Z.-Q., Zhang, L., Wang, Z.-L., and Zhang, L., 2021, Boron and molybdenum isotopic fractionation during crustal anatexis: Constraints from the Conadong leucogranites in the Himalayan Block, South Tibet: *Geochimica et Cosmochimica Acta*, v. 297, p. 120–142, <https://doi.org/10.1016/j.gca.2021.01.005>.
- Fang, W., Dai, L.-Q., Zheng, Y.-F., and Zhao, Z.-F., 2022, Basalt Mo isotope evidence for crustal recycling in continental subduction zone: *Geochimica et Cosmochimica Acta*, v. 334, p. 273–292, <https://doi.org/10.1016/j.gca.2022.08.008>.
- Gale, A., Dalton, C. A., Langmuir, C. H., Su, Y., and Schilling, J.-G., 2013, The mean composition of ocean ridge basalts: *Geochemistry, Geophysics, Geosystems*, v. 14, p. 489–518, <https://doi.org/10.1029/2012GC004334>.
- Guo, Z., and Wilson, M., 2019, Late Oligocene–early Miocene transformation of postcollisional magmatism in Tibet: *Geology*, v. 47, p. 776–780, <https://doi.org/10.1130/g46147.1>.
- Guo, Z., Wilson, M., Dingwell, D. B., and Liu, J., 2021, India-Asia collision as a driver of atmospheric CO<sub>2</sub> in the Cenozoic: *Nature Communications*, v. 12, p. 3891, <https://doi.org/10.1038/s41467-021-23772-y>.
- Huang, C., Gu, H.-O., Sun, H., Wang, F., and Chen, B., 2021, High-precision determination of stable potassium and magnesium isotopes utilizing single column separation and multicollector inductively coupled plasma mass spectrometry: *Spectrochimica Acta Part B: Atomic Spectroscopy*, v. 181, p. 106232, <https://doi.org/10.1016/j.sab.2021.106232>.

- Huang, F., Li, J., Xu, J., Chen, J., Wang, B., Hu, P., Xu, R., Zeng, Y., Zhang, L., and Zhou, T., 2023, Mo isotopes archive oceanic sediments in post-orogenic lithospheric mantle: *Geochimica et Cosmochimica Acta*, v. 341, p. 75-89, <https://doi.org/10.1016/j.gca.2022.11.023>.
- Jackson, M. G., Hart, S. R., Koppers, A. A., Staudigel, H., Konter, J., Blusztajn, J., Kurz, M., and Russell, J. A., 2007, The return of subducted continental crust in Samoan lavas: *Nature*, v. 448, p. 684-687, [10.1038/nature06048](https://doi.org/10.1038/nature06048).
- Li, J., Liang, X. R., Zhong, L. F., Wang, X. C., Ren, Z. Y., Sun, S. L., Zhang, Z. F., and Xu, J. F., 2014, Measurement of the Isotopic Composition of Molybdenum in Geological Samples by MC-ICP-MS using a Novel Chromatographic Extraction Technique: *Geostandards and Geoanalytical Research*, v. 38, p. 345-354, <https://doi.org/10.1111/j.1751-908X.2013.00279.x>.
- Li, S.-G., Yang, W., Ke, S., Meng, X., Tian, H., Xu, L., He, Y., Huang, J., Wang, X.-C., Xia, Q., Sun, W., Yang, X., Ren, Z.-Y., Wei, H., Liu, Y., Meng, F., and Yan, J., 2017, Deep carbon cycles constrained by a large-scale mantle Mg isotope anomaly in eastern China: *National Science Review*, v. 4, p. 111-120, <https://doi.org/10.1093/nsr/nww070>.
- Liang, Y.-H., Halliday, A. N., Siebert, C., Fitton, J. G., Burton, K. W., Wang, K.-L., and Harvey, J., 2017, Molybdenum isotope fractionation in the mantle. *Geochimica et Cosmochimica Acta*, v. 199, p. 91-111, <https://doi.org/10.1016/j.gca.2016.11.023>.
- Lin, Z., Sun, X., Strauss, H., Eroglu, S., Böttcher, M. E., Lu, Y., Liang, J., Li, J., and Peckmann, J., 2021, Molybdenum isotope composition of seep carbonates – Constraints on sediment biogeochemistry in seepage environments: *Geochimica et Cosmochimica Acta*, v. 307, p. 56-71, <https://doi.org/10.1016/j.gca.2021.05.038>.
- Liu, D., Zhao, Z., Zhu, D.-C., Niu, Y., Widom, E., Teng, F.-Z., DePaolo, D. J., Ke, S., Xu, J.-F., Wang, Q., and Mo, X., 2015, Identifying mantle carbonatite metasomatism through Os-Sr-Mg isotopes in Tibetan ultrapotassic rocks: *Earth and Planetary Science Letters*, v. 430, p. 458-469, <https://doi.org/10.1016/j.epsl.2015.09.005>.
- Liu, X.-N., Hin, R. C., Coath, C. D., Bizimis, M., Su, L., Ionov, D. A., Takazawa, E., Brooker, R., and Elliott, T., 2023, The magnesium isotopic composition of the mantle: *Geochimica et Cosmochimica Acta*, v. 358, p. 12-26, <https://doi.org/10.1016/j.gca.2023.08.011>.
- Liu, S. A., Wang, Z. Z., Yang, C., Li, S. G., and Ke, S., 2020, Mg and Zn isotope evidence for two types of mantle metasomatism and deep recycling of magnesium carbonates: *Journal of Geophysical Research: Solid Earth*, v. 125, p. e2020JB020684, <https://doi.org/10.1029/2020jb020684>.
- Liu, S.-A., Qu, Y.-R., Wang, Z.-Z., Li, M.-L., Yang, C., and Li, S.-G., 2022, The fate of subducting carbon tracked by Mg and Zn isotopes: A review and new perspectives: *Earth-Science Reviews*, v. 228, p. 104010, <https://doi.org/10.1016/j.earscirev.2022.104010>.
- McCoy-West, A. J., Chowdhury, P., Burton, K. W., Sossi, P., Nowell, G. M., Fitton, J. G., Kerr, A. C., Cawood, P. A., and Williams, H. M., 2019, Extensive crustal extraction in Earth's early history inferred from molybdenum isotopes: *Nature Geoscience*, v. 12, p. 946-951, [10.1038/s41561-019-0451-2](https://doi.org/10.1038/s41561-019-0451-2).

- McDonough, W. F., Sun, S. & s., 1995, The composition of the Earth. *Chemical Geology*, v. 120, p. 223–253.  
[https://doi.org/10.1016/0009-2541\(94\)00140-4](https://doi.org/10.1016/0009-2541(94)00140-4).
- Pichat, S., Douchet, C., and Albarède, F., 2003, Zinc isotope variations in deep-sea carbonates from the eastern equatorial Pacific over the last 175 ka: *Earth and Planetary Science Letters*, v. 210, p. 167–178,  
[https://doi.org/10.1016/S0012-821X\(03\)00106-7](https://doi.org/10.1016/S0012-821X(03)00106-7).
- Pickard, H., Palk, E., Schönbächler, M., Moore, R. E. T., Coles, B. J., Kreissig, K., Nilsson-Kerr, K., Hammond, S. J., Takazawa, E., Hémond, C., Tropper, P., Barfod, D. N., and Rehkämper, M., 2022, The cadmium and zinc isotope compositions of the silicate Earth – Implications for terrestrial volatile accretion: *Geochimica et Cosmochimica Acta*, v. 338, p. 165–180, <https://doi.org/10.1016/j.gca.2022.09.041>.
- Plank, T., and Manning, C. E., 2019, Subducting carbon: *Nature*, v. 574, p. 343–352, <https://doi.org/10.1038/s41586-019-1643-z>.
- Ritter, X., Sanchez-Valle, C., Sator, N., Desmaele, E., Guignot, N., King, A., Kuppenko, I., Berndt, J., and Guillot, B., 2020, Density of hydrous carbonate melts under pressure, compressibility of volatiles and implications for carbonate melt mobility in the upper mantle: *Earth and Planetary Science Letters*, v. 533, p. 116043, <https://doi.org/10.1016/j.epsl.2019.116043>.
- Romaniello, S. J., Herrmann, A. D., and Anbar, A. D., 2016, Syndepositional diagenetic control of molybdenum isotope variations in carbonate sediments from the Bahamas: *Chemical Geology*, v. 438, p. 84–90, <https://doi.org/10.1016/j.chemgeo.2016.05.019>.
- Rudnick, R.L., and Gao, S., 2003, Composition of the continental crust, in Holland, H.D., and Turekian, K.K., eds., *Treatise on Geochemistry*, Volume 3. The Crust: Amsterdam, Netherlands, Elsevier, 1–64.
- Shu, Z.-T., Liu, S.-A., Prelević, D., Wang, Y., Foley, S. F., Cvetković, V., and Li, S., 2023, Recycled carbonate-bearing silicate sediments in the sources of Circum-Mediterranean K-rich lavas: Evidence from Mg-Zn isotopic decoupling: *Journal of Geophysical Research: Solid Earth*, v. 128, p. e2022JB025135, <https://doi.org/10.1029/2022JB025135>.
- Sun, P., Niu, Y., Duan, M., Chen, S., Guo, P., Gong, H., Xiao, Y., and Wang, X., 2023, Zinc isotope fractionation during mid-ocean ridge basalt differentiation: Evidence from lavas on the East Pacific Rise at 10°30'N: *Geochimica et Cosmochimica Acta*, v. 346, p. 180–191, <https://doi.org/10.1016/j.gca.2023.02.012>.
- Tang, G.-J., Wyman, D. A., Wang, Q., Ma, L., Dan, W., Yang, Y.-N., Liu, X.-J., and Chen, H.-Y., 2022, Links between continental subduction and generation of Cenozoic potassic–ultrapotassic rocks revealed by olivine oxygen isotopes: A case study from NW Tibet: *Contributions to Mineralogy and Petrology*, v. 177, <https://doi.org/10.1007/s00410-022-01920-x>.
- Teng, F.-Z., Wadhwa, M., and Helz, R. T., 2007, Investigation of magnesium isotope fractionation during basalt differentiation: Implications for a chondritic composition of the terrestrial mantle: *Earth and Planetary Science Letters*, v. 261, p. 84–92, <https://doi.org/10.1016/j.epsl.2007.06.004>.
- Teng, F.-Z., 2017, Magnesium Isotope Geochemistry: *Reviews in Mineralogy and Geochemistry*, v. 82, p. 219–287, <https://doi.org/10.2138/rmg.2017.82.7>.

- Vervoort, J. D., Patchett, P. J., Blichert-Toft, J. and Albarède, F., 1999, Relationships between Lu–Hf and Sm–Nd isotopic systems in the global sedimentary system. *Earth and Planetary Science Letters* v. 168, p. 79–99. [https://doi.org/10.1016/S0012-821X\(99\)00047-3](https://doi.org/10.1016/S0012-821X(99)00047-3).
- Voegelin, A. R., Nägler, T. F., Samankassou, E., and Villa, I. M., 2009, Molybdenum isotopic composition of modern and Carboniferous carbonates: *Chemical Geology*, 265, 488–498, <https://doi.org/10.1016/j.chemgeo.2009.05.015>.
- Wang, X.-J., Chen, L.-H., Hofmann, A. W., Mao, F.-G., Liu, J.-Q., Zhong, Y., Xie, L.-W., and Yang, Y.-H., 2017, Mantle transition zone-derived EM1 component beneath NE China: Geochemical evidence from Cenozoic potassic basalts: *Earth and Planetary Science Letters*, v. 465, p. 16–28, <https://doi.org/10.1016/j.epsl.2017.02.028>.
- Wang, Z.-Z., Liu, S.-A., Liu, J., Huang, J., Xiao, Y., Chu, Z.-Y., Zhao, X.-M., and Tang, L., 2017, Zinc isotope fractionation during mantle melting and constraints on the Zn isotope composition of Earth's upper mantle: *Geochimica et Cosmochimica Acta*, v. 198, p. 151–167, <https://doi.org/10.1016/j.gca.2016.11.014>.
- Wang, Z.-Z., Liu, S.-A., Liu, Z.-C., Zheng, Y.-C., and Wu, F.-Y., 2020, Extreme Mg and Zn isotope fractionation recorded in the Himalayan leucogranites: *Geochimica et Cosmochimica Acta*, v. 278, p. 305–321, <https://doi.org/10.1016/j.gca.2019.09.026>.
- Wang, Z.-Z., and Liu, S.-A., 2021, Evolution of Intraplate Alkaline to Tholeiitic Basalts via Interaction Between Carbonated Melt and Lithospheric Mantle: *Journal of Petrology*, v. 62, 10.1093/petrology/egab025.
- Wang, J., Wang, Q., Ma, L., Hu, W.-L., Wang, J., Belousova, E., and Tang, G.-J., 2023, Rapid Recycling of Subducted Sediments in the Subcontinental Lithospheric Mantle: *Journal of Petrology*, v. 64, p. egad056, <https://doi.org/10.1093/petrology/egad056>.
- Willbold, M., Hibbert, K., Lai, Y. J., Freymuth, H., Hin, R. C., Coath, C., Vils, F., and Elliott, T., 2016, High-Precision Mass-Dependent Molybdenum Isotope Variations in Magmatic Rocks Determined by Double-Spike MC-ICP-MS: *Geostandards and Geoanalytical Research*, v. 40, p. 389–403, <https://doi.org/10.1111/j.1751-908X.2015.00388.x>.
- Willbold, M., and Elliott, T., 2017, Molybdenum isotope variations in magmatic rocks: *Chemical Geology*, v. 449, p. 253–268, <https://doi.org/10.1016/j.chemgeo.2016.12.011>.
- Zhao, P.-P., Li, J., Zhang, L., Wang, Z.-B., Kong, D.-X., Ma, J.-L., Wei, G.-J., and Xu, J.-F., 2016, Molybdenum Mass Fractions and Isotopic Compositions of International Geological Reference Materials: *Geostandards and Geoanalytical Research*, v. 40, p. 217–226, <https://doi.org/10.1111/j.1751-908X.2015.00373.x>.
- Zhu, Y.-T., Li, M., Wang, Z.-C., Zou, Z.-Q., Hu, Z.-C., Liu, Y.-S., Zhou, L., and Chai, X.-N., 2019, High-precision copper and zinc isotopic measurements of igneous rock standards using a large-geometry MC-ICP-MS: *Atomic spectroscopy*, v. 40, p. 206–214, <https://doi.org/10.1039/C3JA50232E>.
- Zhang, M.-Y., Huang, C.-C., Hao, L.-L., Qi, Y., Wang, Q., Kerr, A. C., Wei, G.-J., Li, J., Ma, J.-L., Ma, L., and Fan, J.-J., 2023, Light Mo isotopes of post-collisional ultrapotassic rocks in southern Tibet derived from subducted Indian continental crust: *Geochemistry, Geophysics, Geosystems*, v. 24, p. e2023GC011053, <https://doi.org/10.1029/2023GC011053>.